Fast Restoration of Aberration-Degraded Extended Object Based on Local Region Abstraction
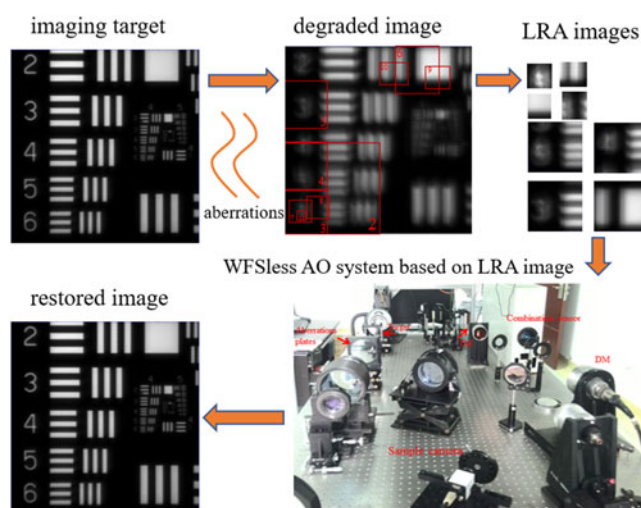
Lianghua Wen
Ping Yang
Shuai Wang
Shanqui Chen
Wenjing LIU
Wei Bai
Zhiqiang Xu
Feilong Wang
Bing Xu

imaging target — degraded image — LRA images — aberrations — WFSless AO system based on LRA image — restored image

◆IEEE

Fast Restoration of Aberration-Degraded Extended Object Based on Local Region Abstraction

Lianghua Wen [1,2,3,4] **Ping Yang,** [1,2] **Shuai Wang,** [1,2] **Shanqui Chen,** [1,2] **Wenjing LIU,** [1,2] **Wei Bai,** [1,2,3] **Zhiqiang Xu,** [1,2,3] **Feilong Wang,** [1,2,3] **and Bing Xu** [1,2]

[1]The Key laboratory of Adaptive Optics, Chinese Academy of Sciences, Chengdu 610209, China
[2]Institute of Optics and Electronics, Chinese Academy of Sciences, Chengdu 610209, China
[3]University of Chinese Academy of Sciences, Beijing 100049, China
[4]School of Physics and Electronic Engineering, Yibin University, Yibin 644000, China

Abstract: The compensating capability of wavefront sensorless adaptive optics (WFSless AO) system for extended object images degraded by aberration is severely limited to correction speed due to largely sized images and low frame rate of camera. To improve the correction capability of WFSless AO system, a method based on local region abstraction (LRA) is presented according to the sparse characteristics of extended object imaging. The experiment results of image restoration with WFSless AO system based on LRA show that the correction speed of this method is 8–20 times faster than that of the previous method for the static aberration, the image restoration speed is improved by about 3.5 times under the dynamic aberration.

Index Terms: Adaptive optics system, image restoration, LRA, correction speed, aberration.

1. Introduction

The images for extended object are inevitably distorted and blurred owing to all kinds of factors in actual imaging system such as the system instability, the assembling errors, the wavefront aberrations, and the thermal effect of imaging components. The restoration and enhancement of degraded images is completed in digital image processing technology such as self-deconvolving data reconstruction algorithm (SeDDaRA) [1]–[3], total variation minimization based on convex optimization [4]. However, it is difficult for these algorithms to be applied in real time imaging system due to complicated computation, massive waste time, demanding hardware requirement, lack of objective evaluating specification, and confining to some special models. Wavefront sensorless adaptive optics (WFSless AO) system has been widely used in some imaging applications, such as microscopy [5], [6], human eyes imaging [7], [8], and remote sensing [9], [10]. The high-resolution images could be acquired by WFSless AO system for compensation the aberrations, which are caused

by the imperfection of imaging system and the distortions on the light beam. It is practicable to incorporate WFSless AO system with imaging system owing to its simple structure. Unfortunately, the performance improvement of imaging with WFSless AO system is confined to the aberrations correction speed due to the large sized images and the limited frame rate of camera. For example, the membrane optic imager real-time exploitation (MOIRE) is a large-aperture transmissive diffractive optical space telescope plan, which could image an area greater than 100 square kilometers with a video update rate of at least one frame per second [11]. WFSless AO system could be used to enhance imaging quality for its simple constitution [12]. However, it is not acceptable that the frame rate is one per second in WFSless AO system. For qualified image acquiring, it is vital to improve the correction speed of WFSless AO system.

In this paper, a method featured with less computation complexity and fast correction speed is proposed, which is based on local region abstraction of images according to the convolution characteristics in extended object imaging processes. Firstly, the essential similarity between restoration progress of SeDDaRA and the imaging with WFSless AO system is analyzed. Then stochastic parallel gradient descent (SPGD) algorithm [13], [14] with LRA images of extended object is proposed according to the integrity of point spread function (PSF) acquired from LRA images. Furthermore, the image size and selection criterion of LRA images are given according to the correction capability of WFSless AO system. Finally, the performance of WFSless AO system with LRA images is analyzed through the several metrics of restored images.

The contribution of our work is that SPGD algorithm with LRA images of extended object is proposed to enhance the aberrations correction speed of WFSless AO system. The remains of this paper are organized as follows. In Section 2, we simply analyze the progress of SeDDaRA [1], [2] and introduce the WFSless AO system. In Section 3 and Section 4, the correction experiments of extended object imaging by SPGD algorithm based on LRA images under the static and dynamic aberrations are presented and discussed respectively.

2. Theoretical Basis

Blind deconvolution algorithms for restoring images from degraded data can be either iterative or non-iterative. The non-iterative algorithms with a little priori knowledge about degradations are the focus of image restoration due to the comparatively easy implementation and wide application for many types' degradations [1], [2]. SeDDaRA is still the important algorithm for the approximately space invariant system, although there are many restoration approaches being developed continuously. The corresponding degradations model can be expressed as follows for a linear space-invariant imaging system.

$$g(x, y) = f(x, y) * d(x, y) + w(x, y) \tag{1}$$

where $g(x, y)$ is degraded image, which can be expressed as the two-dimension convolution of the extended object $f(x, y)$ and the point spread function (PSF) $d(x, y)$ of imaging system with degradations, plus an additive noise term $w(x, y)$. The symbol $*$ is convolution operator.

The image restoration with deconvolution can be expressed as follows.

$$f(x, y) = F^{-1}\left[\frac{G(u, v) - W(u, v)}{D(u, v)}\right] \tag{2}$$

where symbol F^{-1} is inverse Fourier transformation. $G(u, v)$, $D(u, v)$, and $W(u, v)$ are the two-dimension Fourier transformations of blurred image $g(x, y)$, PSF $d(x, y)$, and image noise $w(x, y)$ respectively. The precise acquisition of PSF $d(x, y)$ is the essential problem of image restoration and enhancement. The algorithms about acquiring PSF could be divided into evaluating PSF according to prior knowledge or measurement and blind optimization. A common model of PSF named G
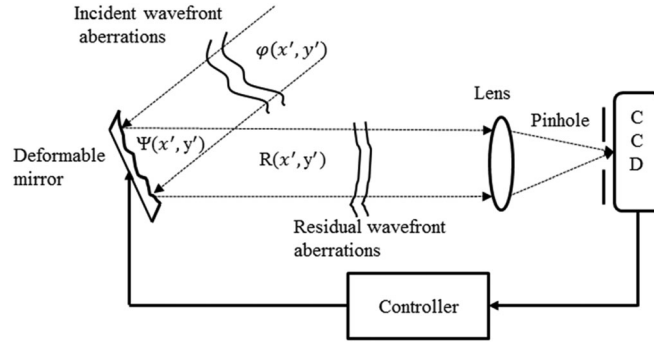
Fig. 1. The schematic of WFSless AO system. The light is depicted as dot line. The control loop is shown as solid line.

class kernel function is capable of indicating many space-invariant linear systems' PSF.

$$D(u, v) = \int_S d(x, y) \exp[-j2\pi(ux + vy)]dxdy$$

$$= \exp[-c(u^2 + v^2)^\beta] \tag{3}$$

where β $(0 < \beta < 1)$ represents the different degradation processes with its different values. For example, the Gauss process is expressed with $\beta = 1$; the ideal imaging process for lens system is approximately featured by $\beta = 3/4$; the degradation owing to atmosphere turbulence is nearly depicted as $\beta = 5/6$ and so on. The degradation degree is featured with c $(c > 0)$. So, the speed and performance of image restorations through deconvolution is greatly dependent on the algorithms of acquiring PSF by either blind optimization or model estimation.

2.1 Restoration With WFSless AO System

Comparing with the restoration using deconvolution after imaging, The WFSless AO system is capable of compensating the wavefront aberrations of imaging beam to improve the system's PSF during the imaging process. Then the high-resolution images could be attained directly in actual imaging system. The schematic of WFSless AO system can be depicted as shown in Fig. 1.

The imaging beam with wavefront aberrations is focused on the focal plane through lens and a pinhole. The camera samples the images and sends the corresponding signals to the controller. The controller manipulates the deformable mirror (DM) to compensate the aberrations of light beam according to image metrics. The aberrations of incident beam are represented as $\varphi(x', y')$, where (x', y') is the pupil plane coordinate. The DM's correction surface shapes are depicted as $\Psi(x', y')$. The expected control objective for WFSless AO system is to minimize the residual aberrations $R(x', y')$ and to improve image quality.

$$R(x', y') = \Psi(x', y') - \varphi(x', y') \tag{4}$$

In the actual imaging systems, the PSF $d(x, y)$ is the far-field image of point object located infinitely remote position according to physical optics [15].

$$d(x, y) = \left| \iint A(x', y') . \exp[jR(x', y')] . \exp^{\frac{jk[(x'-y)^2 + (y'-y)^2]}{2z}} dx' dy' \right| \tag{5}$$

where (x, y) is the rectangular coordinate in the input plane of the camera, $k = 2\pi/\lambda$ is wave number, λ is the wavelength of the input wavefront, z is the focal length of the positive lens, and j is the imaginary unit. $A(x', y')$ is the amplitude of the input wavefront, which is generally set to be unity. Therefore, the image $g(x, y)$ could be restored when the $d(x, y)$ is improved by minimizing the $R(x', y')$

using WFSless AO system. However, the correction speed of WFSless AO system is limited owing to the large sized image and low frame rate of camera. For example, for the monochrome image sized 1024×1024 pixels (maybe larger) with 12 bits per pixel; generally, cameras just can work at dozens of frames per second. Especially for some imaging wave length, it is difficult to enhance the frame rate owing to the low quantum efficiency of image sensor. Even if the high speed scientific camera is available as the developing of photon-electronic technique, it is subjected to the hundreds of thousands dollars' expense at least. Additionally, the data transmission width and computation burden will increase sharply as the rising of fame rate. On the contrary, it is urgent need for high frame rate to improve the correction speed of WFSless AO system under the dynamic aberration. Fortunately, the sparse characteristics of image restoration are beneficial to raise the correction speed for WFSless AO system.

2.2 The Sparse in Restoration

For a special imaging system with linear space-invariance, the performance of system is depicted with PSF that is the sparse expression of imaging process. The issue of the image restoration with deconvolution is to precisely evaluate PSF by model or priori knowledge. The essential of WFSless AO system is to optimize the PSF through compensating the wavefront aberrations of imaging beam. The sparse expression of degradation is the Fourier transform of the PSF $d(x, y)$.

$$D^{1-\alpha}(u, v) = K_D S\{|S_G(u, v) - S_W(u, v)|^{\alpha/2}\} \tag{6}$$

$$S_G(u, v) = \frac{|F[g(x, y)]|^2}{N * M} \tag{7}$$

$$S_W(u, v) = \frac{|F[w(x, y)]|^2}{N * M} \tag{8}$$

where $S\{\ldots\}$ is smoothing operator, K_D is a proportion term, $S_G(u, v)$ and $S_W(u, v)$ are the power spectral density of degraded image sized $M \times N$ and noise respectively. The symbol F represents Fourier transform. Some confine conditions for the sparse characteristics are discussed in reference [1], [2]. So PSF could be approximately abstracted in the small segments of degraded image $g(x, y)$, which includes the integral information about PSF. In other words, the PSF is improved efficiently with WFSless AO system based on sub-image of $g(x, y)$ including an integral PSF at least. This is important for raise the camera frame rate by reducing the sampling window size.

2.3 LRA

According to the sparse characteristics of image degradation analyzed above, WFSless AO system based on LRA images of the degraded image for extended object is presented to improve the correction speed. The essential of WFSless AO system is to improve the PSF by correcting the aberrations. Then the image is restored according to the convolution process of PSF and the extended object shown as Eq. (1). For a linear space-invariant system, the nature of convolution is the superposition of the images of all the point sources forming the extended object, which are the PSFs with different space shifts. Therefore, any one PSF acquired from the degraded image could be regarded as the optimization target of WFSless AO system. It is equivalent that the any sized local image including an integral PSF at least can be the input of WFSless AO system. So WFSless AO system based on LRA images is depicted as Fig. 2. The small sized local region images of extended object are sampled by camera CCD2 and delivered to controller for optimization algorithms. Generally, the frame rate is inverse proportion to the imaging sensor's window size of local region image. The camera CCD1 is used to sample the large sized full view-field image of extended object at low frame rate. Considering the high frame rate demands of optimization control and the large sized image acquiring, the image sampling is completed by two different cameras.
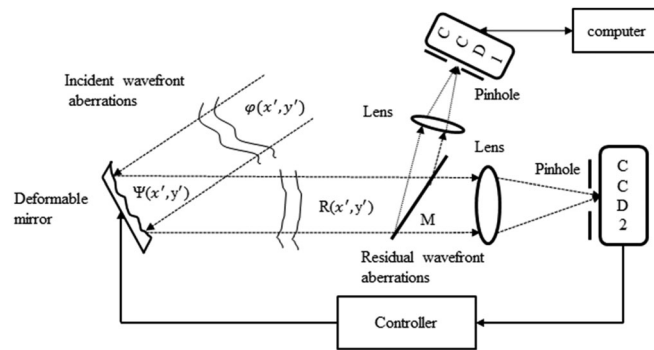
Fig. 2. The schematic of WFSless AO system based LRA. The light is depicted as dot line. The control loop is shown as solid line.
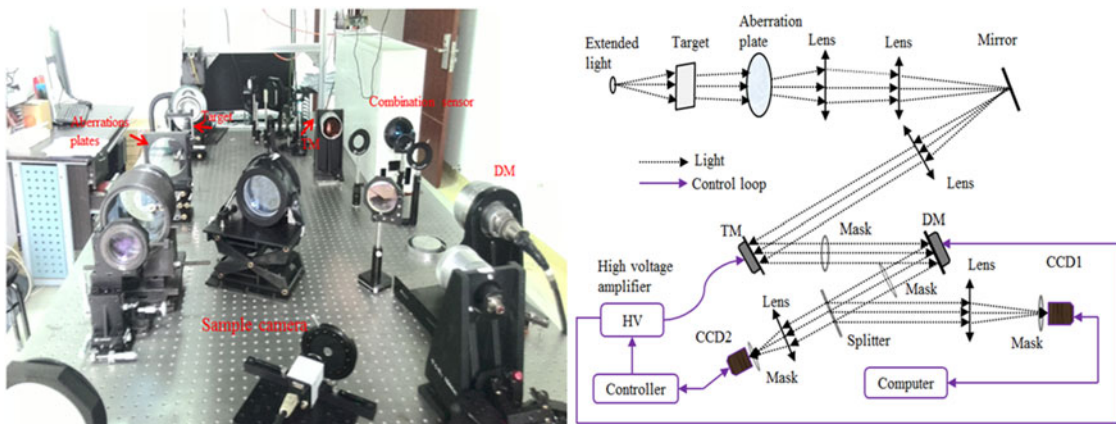

Fig. 3. The experimental system for image restoration.

To verify the performance of this method, the experiments about degraded image restoration under static aberrations and dynamic aberrations are introduced respectively in subsequent sections.

3. Static Restorations

The experiment system for image restoration with WFSless AO system is set up as Fig. 3. The system is mainly composed by an extended light source, an extended target (USAF1951), an optical beam shrinker, a tilt/tip mirrors (TM), a deformable mirror (DM), a computer control system, and a combination sensor. The combination sensor consists of a Shack-Hartmann sensor, a near-field detection camera, and a far-field measurement camera. The LRA images of extended object and the feedback signal to the control computer are completed by the far-field camera of the combination sensor in WFSless AO system.

The images are degraded by the distortions of the aberration plate and system's initial aberrations. These aberrations are compensated by DM according to the driver voltages generated during the iterations of control algorithm to optimizing the LRA images. The input wavefront aberrations $\varphi(x', y')$ and the DM's correction shapes $\Psi(x', y')$ are expressed as the series of M orthonormal functions and N orthonormal functions respectively.

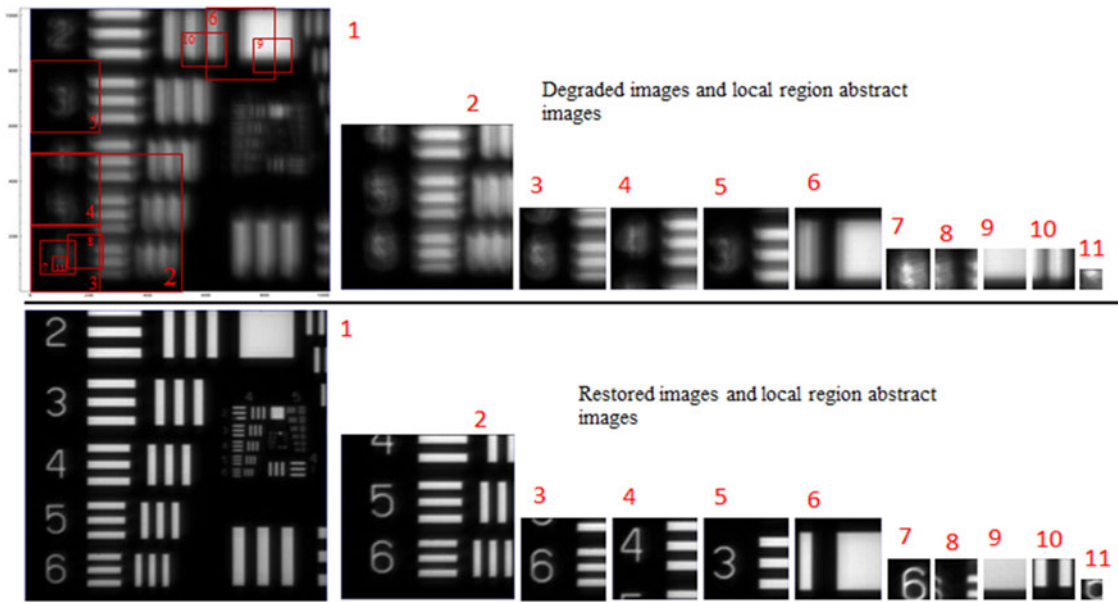$$\varphi(x', y') = \sum_{i=1}^{M} a_i Z_i(x', y') \tag{9}$$

Fig. 4. The LRA images with degradation and restoration.

$$\Psi(x', y') = \sum_{i=1}^{N} \beta_i Z_i(x', y') \tag{10}$$

where $Z_i(x', y')$ is the i order Zernike basis function, whose coefficients are β_i and a_i in the wavefront aberrations and correction shapes respectively. In image restoration experiments, SPGD algorithm with LRA images of the extended object is adopted in WFSless AO system. The implementation of SPGD based on aberration mode is indicated as following.

$$\alpha^{(k+1)} = \alpha^{(k)} + \gamma.\Delta\alpha^{(k)}.\Delta J^{(k)} \tag{11}$$

$$\Delta J^{(k)} = J(\alpha^{(k)} + \Delta\alpha^{(k)}) - J(\alpha^{(k)} - \Delta\alpha^{(k)}) \tag{12}$$

$$v = C_{zv} a \tag{13}$$

where $\alpha^{(k)} = (\alpha_1^{(k)}, \alpha_2^{(k)} \cdots \alpha_N^{(k)})$ is comprised by the coefficients of N Zernike basis functions at time K. $\alpha^{(k+1)}$ is the corresponding vector at time $K+1$, $\Delta\alpha^{(k)}$ is a random disturbing conformed to the Bernoulli distribution. γ represents the step gain. $\Delta J^{(k)}$ is the gradient estimation of $J^{(k)}$ calculated from image $I(x, y)$ at time K, which is the difference between $J(\alpha^{(k)} + \Delta\alpha^{(k)})$ and $J(\alpha^{(k)} - \Delta\alpha^{(k)})$ when the voltages corresponding to $(\alpha^{(k)} + \Delta\alpha^{(k)})$ and $(\alpha^{(k)} - \Delta\alpha^{(k)})$ are imposed on DM respectively. C_{zv} is the correlation matrix with $Q * N$ dimensions between the DM with Q driver elements and N Zernike basis functions. The index of LRA image $I(x, y)$ is named image sharpness and defined as following

$$J = \frac{\sum I^2(x, y)}{\left(\sum I(x, y)\right)^2} \tag{14}$$

The LRA images are acquired by setting the different configurations for window size and window location in camera CCD2, which are demonstrated as Fig. 4. The degraded LRA images and the restored LRA images are numbered from 1 to 11, which are named from LRA1 to LRA11. The size of LRA1 image is 1024 × 1024 pixels, and the size of LRA2 image is 512 × 512 pixels.
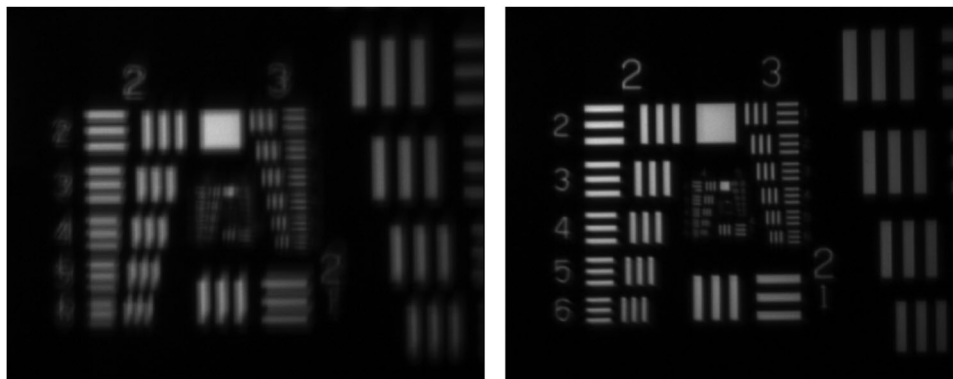
Fig. 5. The whole image of extened object with degradations and restoration: the left is degraded image and the right is restored imge with WFSless AO sytem.

LRA3–LRA6 images have the same size with 256×256 pixels located in the different regions of the extended object image. LRA7–LRA10 images sized 128×128 pixels are the different segments of the extended object image. LRA11 image is the smallest size with 64×64 pixels. The frame rate of camera CCD2 with LRA1 image sized 1024×1024 is only 56 frames per second; however, the frame rate with LRA11 sized 64×64 is more than 1200 frames per second. Although LRA images sampled by camera CCD2 are different, the LRA images are improved evidently with WFSless AO system.

The full field of view image of extended object is acquired by camera CCD1 at the fixed frame rate and varied exposure time, whose parameters configuration is independent on the control system. The full field of view image degraded by static aberrations is shown as Fig. 5, whose resolution is at 4.00 lp/mm. The resolution of the corresponding restored image by WFSless AO system with LRA1 image is up to 20.16 lp/mm. This result shows WFSless AO system is able to improve greatly imaging performance.

In order to compare the convergence speed by WFSless AO system with different LRA images, the image sharpness J defined in Eq. (14) and the image gradient G of LRA images $I(x, y)$ are calculated and recorded in real time during optimizing progress. The image gradient G is defined as following.

$$G = \frac{1}{pq} \sum_{x=1, y=1}^{p,q} (I(x, y) - I_0)^2 \tag{15}$$

Where $I_0 = (1/pq) \sum_{x=1, y=1}^{p,q} I(x, y)$ is the mean of all the pixels gray level, and $p \times q$ is the image size. The image sharpness J curves and the gradient G curves of LRA images sized 1024×1024 pixels, 512×512 pixels, 256×256 pixels, 128×128 pixels, and 64×64 pixels respectively are shown in Figs. 6–Fig. 7. These LRA images are LRA1, LRA2, LRA6, and LRA7and LRA11shown in Fig. 4.

The image sharpness curves and image gradient curves demonstrate that the different size of LRA images result in the distinct value of image sharpness and image gradient during the restoration, and the convergence frames number becomes less firstly as the reduction of LRA images' size, then gradually rises. The frame rate of camera is different for sampling the different size LRA images, so the convergence times with different LRA images is listed in Table 1.

The restoration time of WFSless AO system using LRA1 image is about 42.86 seconds when the camera CCD2 samples the images with 1024×1024 pixels at 56 frames per second. The time is reduced by nearly 20 times with LRA6 image with 256×256 pixels; although the frame rate is just enhanced about 5 times comparing to 56 frames per second. It is beneficial to the shortening the time interval between the control and the signals' acquiring. Generally, the restoration speed
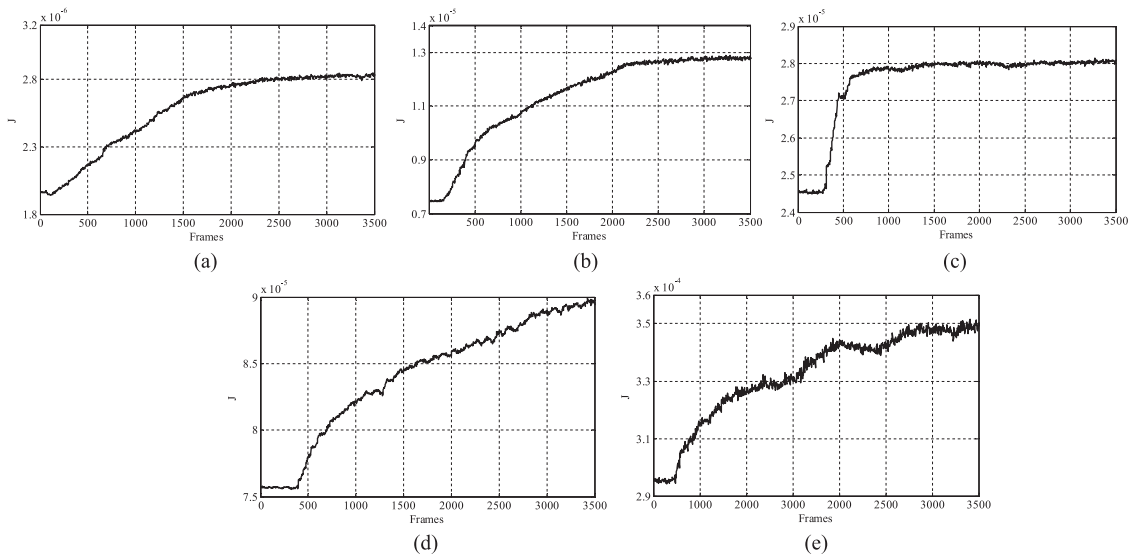
Fig. 6. The image sharpness curves of LRA1, LRA2, LRA6, LRA7, and LRA11 shown in Fig. 6(a)–Fig. 6(e) in sequence.
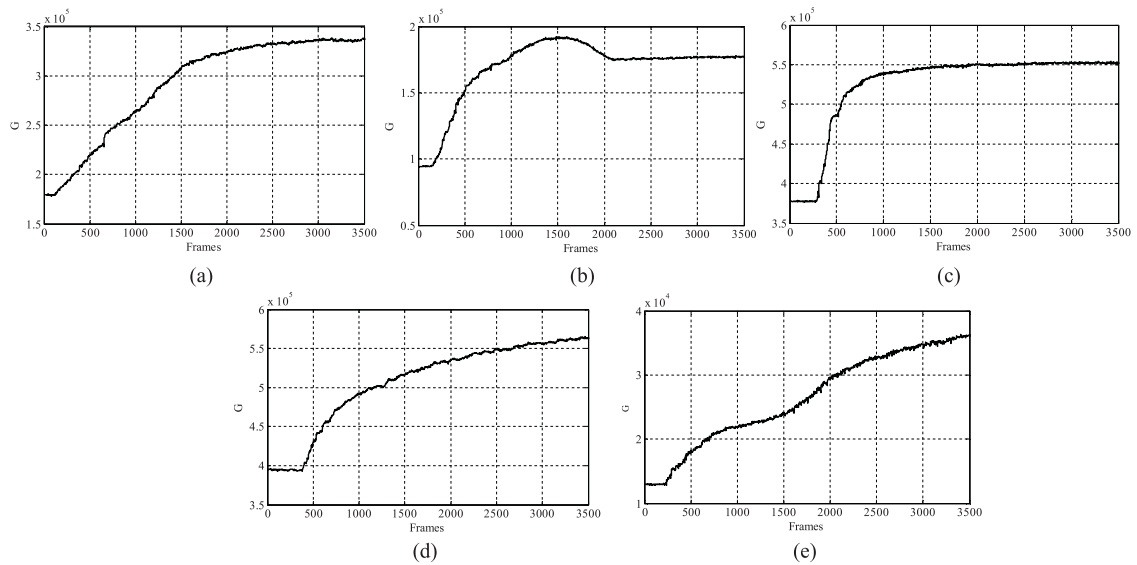

Fig. 7. The gradient curves of LRA1, LRA2, LRA6, LRA7, and LRA11 shown in Fig. 7(a)–Fig. 7(e) in sequence.

is faster and the size of LRA images is smaller. However, the optimum LRA image is LRA6 with 256×256 pixels rather than the smallest sized LRA11 image with 64×64 pixels. The tradeoff between the enhancement of camera's frame rate due to small LRA images and the degradation of estimation PSF of small size LRA image must be considered seriously.

The structure similarity of images is adopted to evaluate the image restoration equivalence with WFSless AO system using different LRA images. The structure similarity of images is defined as following.

$$SI = \frac{(2\mu_x\mu_y + C_1)(2\sigma_{xy} + C_2)}{(\mu_x^2 + \mu_y^2 + C_1)(\sigma_x^2 + \sigma_y^2 + C_2)} \qquad (16)$$

TABLE 1

The Correction Speed Analysis With Different LRA Images

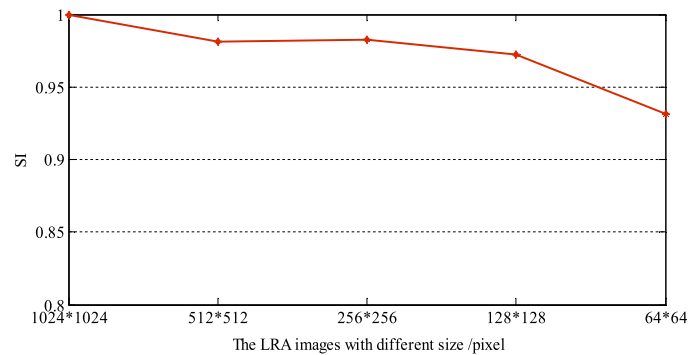| LRA images	Size(pixel)	Frame rate(frames/s)	Convergence frames(frame)	Convergence time (s)
LRA1	1024×1024	56	2400	42.86
LRA2	512×512	128	2200	17.18
LRA6	256×256	288	670	2.33
LRA7	128×128	580	3200	5.52
LRA11	64×64	1220	6800	5.58

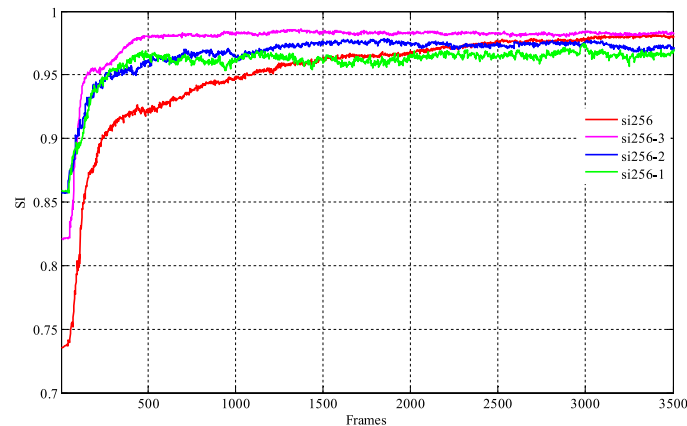Fig. 8. The structure similarity of images.

Fig. 9. The structure similarity of different LRA images sized 256×256 pixels: the legends of structure similarity curves for LRA3–LRA6 are "si256", "si256-1", "si256-2", and "si256-3" in sequence.

Where μ_x and μ_y are the mean value of pixels level in two different images respectively. σ_{xy} is the corresponding covariance. σ_y and σ_y are the corresponding standard variance. The constants C_1 and C_2 are used to make the denominator in Eq. (16) nonzero. The structure similarity of images restored with different LRA images is demonstrated in Fig. 8, which are acquired by camera CCD1, and have the same size.

Although the image structure similarity becomes worse as the reduction of LRA images' size from the curves shown in Fig. 8. It is acceptable that the image structure similarity is more than 0.95, because the inevitable block mismatching of images brings non-negligible computation error.
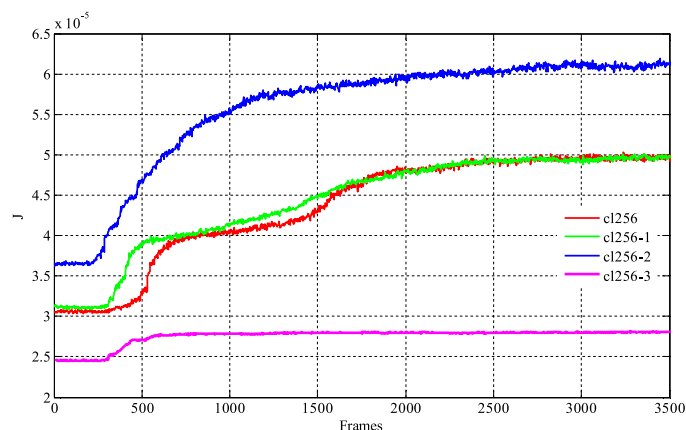
Fig. 10. The image sharpness of different LRA images sized 256 × 256 pixels: the legends of image sharpness curves for LRA3–LRA6 are "cl256", "cl256-1", "cl256-2", and "cl256-3"in sequence.
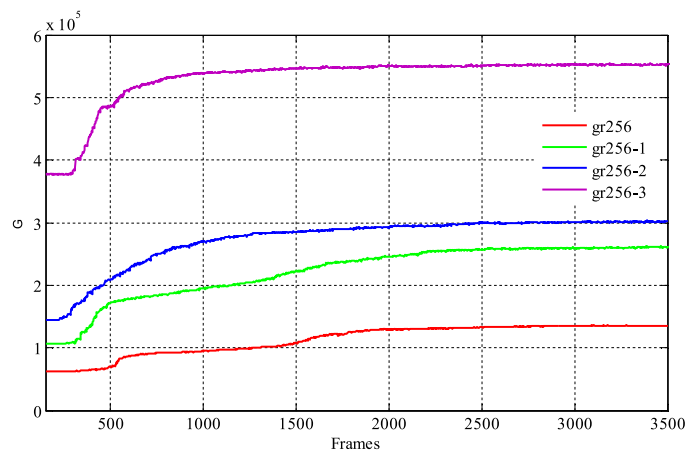

Fig. 11. The gradient of different LRA images sized 256 × 256 pixels: the legends of gradient curves for LRA3–LRA6 are "gr256", "gr256-1", "gr256-2", and "gr256-3" in sequence.

TABLE 2

The Correction Speed Analysis With Different LRA Images

LRA images	Peak pixel level(ADU)	PSNR (dB)	Level mean(ADU)	Structure similarity	Convergence frames(frame)	Convergence time (s)
LRA3	1108	4.26	249.52	0.981	1520	5.27
LRA4	1320	4.99	319.59	0.967	1480	5.13
LRA5	1520	5.67	321.46	0.977	1200	4.16
LRA6	1920	6.68	786.79	0.984	670	2.33

Therefore, LRA6 image with 256 × 256 pixels is the best region image for the image restoration with WFSless AO system according to the corrections speed and the image structure similarity.

To analyze restoration capability with WFSless AO system using the same size LRA images with different positions, the restoration experiments using LRA3, LRA4, LRA5 and LRA6 images are completed respectively, and the corresponding metrics curves and the result analysis are shown in Figs. 9–11and Table 2.
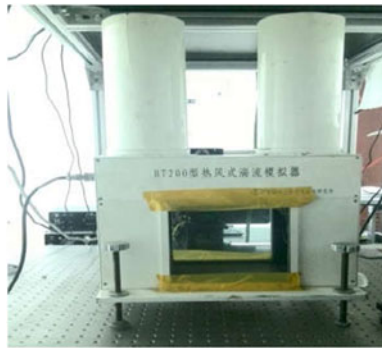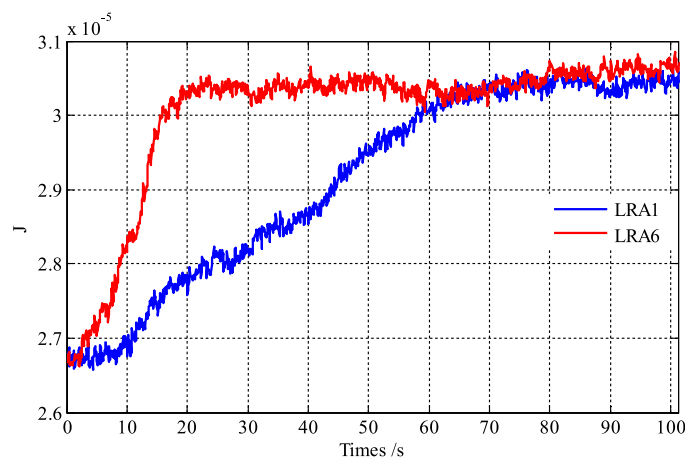
Fig. 12. The simulator of turbulence in hot air.

Fig. 13. The image sharpness of restored images under the dynamic aberrations.

The convergence time with different LRA images ranges from 2.33 sends to 5.27 seconds. The image structure similarity is almost equal. This difference is mainly caused by the different distribution of pixels level in LRA images that can be featured with peak value of pixel level, peak signal noise ratio (PSNR), and mean level of pixels in the different LRA images. It is reasonable according to Eq. (1) that the estimation and correction of PSF is more precise as the improvement of PSNR. Here the selection method of LRA images is presented, that the LRA image with the high peak pixel level, and maximum PNSR is most optimum region images for WFSless AO aberrations correction. The speed of restoration image degraded by static aberrations is enhanced by 8–20 times using LRA images. This is significant for restoration images degraded by dynamic aberrations in practical applications.

4. Dynamic Restoration

To verify the improvement of WFSless AO system using LRA images under the dynamic aberrations, the turbulence simulator shown in Fig. 12 is used to generate the dynamic aberrations and to replace the aberrations plate used in static restoration experiment. The dynamic aberrations are produced by heating and fanning the airflow. Then the image is distorted and blurred by the dynamic aberrations when the airflow temperature ranges from 20 to 45 degrees Celsius and the wind velocity is 3 m/s. The images are drastically distorted as the dynamical aberrations caused by the turbulence in different temperatures. Therefore, the correction speed of WFSless AO system is vital for image
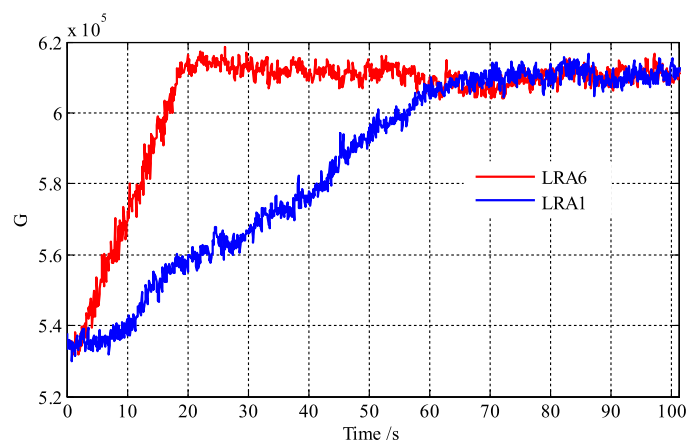
Fig. 14. The gradient of restored images under the dynamic aberrations.

restoration under the dynamic aberrations. The image sharpness and gradient of images restored with WFSless AO system using LRA1 image and LRA6 image respectively under the dynamical aberrations are shown in Figs. 13–14, which are calculated from the full view-field images sampled by camera CCD1 during more than 100 seconds.

The image is improved greatly by WFSless AO system using LRA6 image sized 256×256 pixels after 20 seconds. On the contrary, the system with LRA1 image sized 1024×1024 pixels takes more than 70 seconds to attain the equivalent restored image. The convergence speed of images restoration with LRA6 image is about 3.5 times than using the LRA1 image from the image sharpness curves and the gradients curves. The fluctuations of image sharpness and gradient are evident during the restoration process due to the variation of aberrations as the temperature changing, which is embodied in the bolder curves width. This is distinctly different from the restoration under the static aberrations discussed in previous sections.

5. Conclusion

According to sparse characteristic of image degradations about linear space invariant system, a method based on local region abstraction images is presented by analyzing the essential and similarity of the deconvolution optimizations, and the aberrations correction with WFSless AO systems. Some preliminary selection criterion for LRA images are given and verified in experiments. In restoration images degraded by static aberrations, the speed of restorations with WFSless AO system using LRA images is enhanced by 8–20 times. The corresponding correction speed in dynamics aberrations experiment is improved by about 3.5 times. It could be enhanced greatly by subsequent optimizations. The reduction of LRA images size is beneficial to data transmission and real time control. These advantages are significantly important for large aperture and light-weight imaging system in space telescope or remote sensing in near future.

References

[1] J. N. Caron, N. M. Namazi, R. L. Lucke, C. J. Rollins, and P. R. Lynn Jr., "Blind data restoration with an extracted filter function," *Opt. Lett.*, vol. 26, no. 15, pp. 1164–1166, 2001.
[2] J. N. Caron, N. M. Namazi, and C. J. Rollins, "Noniterative blind data restoration by use of an extracted filter function," *Appl. Opt.*, vol. 41, no. 32, pp. 6884–6885, 2002.
[3] S. Yousaf and S. Yinqin, "Blur kernel optimization: Blur kernel optimization with contrast levels and effectual patch selection using SURF features," in *Proc. IEEE Int. Conf. Imag. Syst. Techn.*, 2013, 337–342 .
[4] A. Beck and M. Teboulle, "Fast gradient-based algorithms for constrained total variation image denoising and deblurring problems," *IEEE Trans. Image Process.*, vol. 18, no. 11, pp. 2419–2433, Nov. 2009.

[5] D. D'ebarre, E. J. Botcherby, T. Watanabe, S. Srinivas, M. J. Booth, and T. Wilson, "Image-based adaptive optics for two-photon microscopy," *Opt. Lett.*, vol. 34, no. 8, pp. 2495–2497, 2009.

[6] A. J. Wright, S. P. Poland, J. M. Girkin, C. W. Freudiger, C. L. Evans, and X. S. Xie, "Adaptive optics for enhanced signal in CARS microscopy," *Opt. Exp.*, vol. 15, no. 26, pp. 18209–18219, 2007.

[7] H. Hofer, N. Sredar, H. Queener, C. Li, and J. Porter, "Wavefront sensorless adaptive optics ophthalmoscopy in the human eye," *Opt. Exp.*, vol. 19, no. 15, pp. 14160–14171, 2011.

[8] L. Ning *et al.*, "A small adaptive optical imaging system for cells of living human retina," *Acta Optica Sinica*, vol. 24, no. 9, pp. 1153–1158, 2004.

[9] Y. Xin, H. Xingzi, and H. Xinqi, "Wavefront sensorless adaptive optics correlation for high-resolution space remote sensing system," *Acta Optica Sinica*, vol. 31, no. 9, pp. 0900118–0900121, 2011.

[10] M. Toyoshima and K. Araki, "In-orbit measurements of short term attitude and vibrational environment on the engineering test satellite VI using laser communication equipment," *Opt. Eng.*, vol. 40, pp. 827–829, 2001.

[11] D. Waller "MOIRE primary diffractive optical element structure deployment testing," *AIAA Sci. Technol.*, vol. 1836, pp. 1–10, 2015.

[12] R. Hansen "Developing lightweight optics for space," *Sci. Technol. Rev.*, vol. 1, no. 3, pp. 20–23, 2013.

[13] M. A. Vorontsov, G. W. Carhart, and J. C. Ricklin, "Adaptive phase-distortion correction based on parallel gradient-descent optimization," *Opt. Lett.*, vol. 22, no. 12, pp. 907–909, 1997.

[14] M. A. Vorontsov and V. P. Sivokon, "Stochastic parallel gradient descent technique for high-resolution wave front phase-distortion correction," *Opt. Soc. Amer. A.*, vol. 15, no. 11, pp. 2745–2758, 1998.

[15] J. W. Goodman, *Introduction to Fourier Optics*. New York, NY, USA: W. H. Freeman & Co Ltd., 2005.